metals

Article

Optimizing Annealing Temperature Control for Enhanced Magnetic Properties in Fe-Si-B Amorphous Flake Powder Cores

Hea-Ran Kim [1,2,†], Dongsup Lee [3,†], Sangsun Yang [1], Young-Tae Kwon [1], Jongryoul Kim [3], Yunseok Kim [2] and Jae-Won Jeong [1,*]

1 Metal Powder Department, Korea Institute of Materials Science (KIMS), 797 Changwondae-ro, Seongsan-gu, Changwon 51508, Republic of Korea; hearan@kims.re.kr (H.-R.K.); nanoyang@kims.re.kr (S.Y.)
2 Department of Materials Science and Engineering, Sungkyunkwan University (SKKU), 2066 Seobu-ro, Yulcheon-dong, Jangan-gu, Suwon 16419, Republic of Korea
3 Department of Materials Science and Chemical Engineering, Hanyang University, Ansan 15588, Republic of Korea; dongsup@ysbiz.co.kr (D.L.)
* Correspondence: jeongjw1204@kims.re.kr
† These authors contributed equally to this work.

Abstract: In this study, we examined the optimal pre- and post-annealing conditions for soft magnetic composites (SMCs) using amorphous flake powders produced through ball milling of amorphous Fe-Si-B ribbons, leading to enhanced magnetic properties. The SMCs, which utilized flake powders created via melt spinning, displayed outstanding DC bias characteristics, as well as increased permeability, primarily due to high saturation magnetization and the flaky morphology of the powders. Pre-annealing was performed not only to remove residual stress formed during the melt spinning process but also to improve pulverizing efficiency, which ultimately affected the particle size of the flake powders. Core annealing was performed to reduce core losses and improve permeability by relieving the residual stress generated during the pressing process. As a result, pre-annealing and core annealing temperatures were identified as crucial factors influencing the magnetic properties of the SMCs. We meticulously analyzed the particle size, the morphology of the flake powder, and the magnetic properties of the SMCs in relation to the annealing temperatures. In conclusion, we demonstrated that flake powder SMCs achieved superior soft magnetic properties, including significantly reduced core loss and heightened permeability, through optimal pre- and core-annealing at 370 °C and 425 °C, respectively.

Keywords: soft magnetic composites; magnetic powder cores; amorphous flake shape powders; soft magnetic properties; pre-annealing temperature; core annealing temperature

Citation: Kim, H.-R.; Lee, D.; Yang, S.; Kwon, Y.-T.; Kim, J.; Kim, Y.; Jeong, J.-W. Optimizing Annealing Temperature Control for Enhanced Magnetic Properties in Fe-Si-B Amorphous Flake Powder Cores. *Metals* **2023**, *13*, 2016. https://doi.org/10.3390/met13122016

Academic Editor: Eric Hug

Received: 30 October 2023
Revised: 7 December 2023
Accepted: 9 December 2023
Published: 15 December 2023

1. Introduction

Inductors are essential components in electronic devices and play a significant role in electronic circuits by facilitating the interconversion of electromagnetic energy [1–3]. As power density in electronic devices continues to increase, the use of inductors with soft magnetic composites (SMCs) is becoming more prevalent, as they offer advantages in miniaturizing components. SMCs can effectively reduce eddy current loss due to insulation between the powders because they are produced by molding the metallic powders coated with surface insulation [4]. Furthermore, the powder form allows for easy application in the manufacturing of complex 3D shapes, including C-type and E-type cores [5].

Generally, SMCs have been implemented using crystalline soft magnetic alloy powders such as FeSi, FeNi, and FeSiAl [6]. However, with the recent increase in operating frequencies of power conversion devices, materials with high ferromagnetic resonance (FMR) are needed that exhibit high permeability and low core loss at higher frequencies [7]. Amorphous alloys have zero magnetic crystal anisotropy and a very homogeneous and isotropic microstructure because it has no crystal defects (voids, dislocations, grain boundaries, inclusions, etc.) and thus exhibits high permeability and low coercivity [8,9]. Moreover, these alloys are suitable for high-frequency materials because their disordered atomic arrangement results in a high electrical resistivity, leading to low eddy current loss during AC magnetization [10]. Furthermore, it is worth noting that amorphous alloys can serve as precursors that can be transformed into a nanocrystalline phase through heat-treatment-induced crystallization. This nanocrystalline phase is known to exhibit superior soft magnetic properties compared to the amorphous materials [11,12]. Among amorphous alloys, $Fe_{78}Si_9B_{13}$ is commercially available and can be mass-produced. For example, Metglas® 2605SA1 has a high saturation magnetization of 1.56 T, high permeability, and very low core loss [13].

Mechanical alloying has the advantage of being able to synthesize materials of a variety of stable and metastable states [14]. However, severe defects and contamination are formed due to plastic deformation and long period of processing, which can result in a deterioration of the magnetic properties of the materials [15,16]. The gas atomization process is known for producing amorphous powder with spherical morphology, which is beneficial due to its near-zero magnetic anisotropy and high filling factor [17]. To achieve an amorphous state, a cooling rate of 10^5 K/s or higher is required [18]. However, gas atomization is characterized by a relatively low cooling rate, ranging from 10^2 to 10^5 K/s [19]. Consequently, alloys suitable for the gas atomization process must possess a high glass-forming ability (GFA), achieved through the inclusion of significant quantities of metalloid elements. As a result, the Fe content in the alloy is limited to less than 80 at.%, leading to a low saturation magnetization of less than 1.6 T for the spherical amorphous powder [20]. In contrast, amorphous ribbons produced using the melt spinning process can achieve high saturation magnetization due to their cooling rate of 10^6 K/s or more. However, to convert the ribbon form into powder form, an additional pulverization process is necessary, as the melt spinning process yields ribbons.

As-fabricated amorphous metal ribbons are difficult to pulverize into powders due to their high toughness. Performing pre-annealing before the milling process can make the ribbons more brittle, thereby increasing pulverization efficiency and subsequently reducing particle size. It is known that annealing effects, including structural relaxation or free volume annihilation, residual stress relief, or short-range ordering and crystallization, increase brittleness [21]. Annealing below the crystallization temperature of amorphous alloys causes structural relaxation and short-range order changes, which closely affect the mechanical properties of amorphous metals. Generally, amorphous metals become more brittle as the annealing temperature and duration increase, when the temperature remains below the crystallization threshold [22]. As such, the pre-annealing temperature should be sufficiently high to enhance pulverization efficiency but must not exceed the crystallization temperature. As the pre-annealing temperature of the amorphous ribbon increases, the pulverization efficiency improves and the particle size after the pulverization decreases. However, prolonged milling time can lead to surface degradation and oxidation, which in turn can cause an increase in coercivity. On the other hand, pre-annealing of an amorphous alloy can reduce the coercivity and improve the permeability by removing the residual stress generated during rapid quenching [23,24].

Reduction in particle size leads to more energy being applied to the surface during the pulverization process. A portion of this energy remains as residual stress and leads to crystal defects and lattice distortion, which in turn cause domain pinning effect, which increases the coercivity and hysteresis loss of the powder core [25]. Therefore, reduction in the particle size through a pulverization process increases the hysteresis loss [26], whereas the intra-particle eddy current loss decreases [27]. Therefore, the temperature of pre-annealing is a factor that greatly affects the core loss of powder cores.

Additionally, the pulverized ribbon becomes a flake powder with a low demagnetization field. The demagnetizing field tends to decrease with an increase in the length and decrease in the thickness of the particles [28]. Furthermore, the demagnetization field of the samples can be manipulated by adjusting the milling conditions, thereby influencing the shape of the flake powders [29].

Residual stress generated during the powder compaction process can also lead to deterioration of soft magnetic properties of SMCs, including increased coercivity and decreased permeability [30]. To achieve optimal soft magnetic properties, it is necessary to perform a core annealing process to remove the residual stress. Residual stress can induce local anisotropy in the amorphous structure since chemical short-range ordering (CSRO), similar to the atomic arrangement regularity of the crystal structure, occurs more frequently [31]. This local anisotropy increases coercivity, which adversely affects soft magnetic properties. Annealing above the Curie temperature eliminates the induced magnetic anisotropy and leads to a disordered spin arrangement. Therefore, annealing above the Curie temperature and rapid cooling are required to suppress the formation of locally induced magnetic anisotropy and to achieve superior soft magnetic properties in composites. It is thus essential to perform core annealing below the crystallization temperature because the crystallization significantly deteriorates soft magnetic properties of amorphous alloys.

It is widely recognized that material properties including powder morphology and processing parameters such as compaction pressure and temperature, along with annealing temperature and duration, significantly impact the performance of amorphous powder cores [32–34]. While numerous studies have explored the effects of annealing on the structural relaxation and brittleness of amorphous materials [35,36], there is a research gap concerning pulverization efficiency and the size and shape of powders according to process conditions. Furthermore, a comprehensive examination of the relationship between soft magnetic properties and process conditions, especially for annealing, has been lacking, making it difficult to derive the optimal process conditions.

In this study, we closely examined the effects of temperature control during pre-annealing and core-annealing on the properties of flake powders and SMCs and determined the optimal temperature conditions. We prepared flake powders through pre-annealing and pulverization of Fe-Si-B amorphous ribbons and, via high-pressure compaction, fabricated toroidal-shaped cores using the pulverized powders. Specifically, we investigated particle size and shape in relation with the pre-annealing temperature, and thoroughly examined their impact, along with that of core annealing, on the soft magnetic properties of the core. We also analyzed the core loss mechanism and its causes by separating it into hysteresis loss and dynamic loss components and in-depth analysis. Finally, through microstructure control and residual stress relaxation in SMCs manufactured using flake powder, we assessed the influence of temperature control during pre-annealing and core annealing on magnetic properties.

2. Experimental Sections

2.1. Materials

$Fe_{78}Si_9B_{13}$ ribbons were supplied by Metglas®, Inc., Co., (Conway, SC, USA). Potassium silicate solutions, for use as binders, were purchased from Young Il chemical Co., (PS-200, Incheon, Republic of Korea). Kenolube, for use as lubricant, was purchased from KenolKobil Co., (Nairobi, Kenya, East Africa).

2.2. Fabrication

Fe-Si-B ribbons were annealed in argon atmosphere at 350–400 °C for 1 h prior to ball milling. When the furnace was set to each heat treatment temperature, the ribbons were placed and air-cooled after 1 h. The pre-annealed ribbon was placed in a milling jar with a ball-to-powder ratio of 20:1. The jar was sealed under argon atmosphere. Then, ball milling was performed at 130 RPM for 24 h. The pulverized powder was sieved to less than 105 μm. Potassium silicate solution at 15.65 vol.% was added to the pulverized powder. Then, evaporation was performed at 90 °C for 5 min, the same time as the mixing. Kenolube at 0.5 wt.% of as lubricant was mixed into the dried powder. Prepared powder was pressed at a pressure of 1.5 GPa for 5 min; it formed a toroidal core with an inner diameter of 15 mm and an outer diameter of 25 mm. The toroidal cores were cured at

150 °C for 1 h in vacuum. Then, each sample was subjected to core annealing at 400–500 °C for 1 h in argon atmosphere. Similar to the pre-annealing process, the sample was placed in a high-temperature furnace and cooled in air. Here, toroidal samples pre-annealed at x °C are denoted as "Px" and toroidal samples core annealed at x °C are denoted as "Cx". Toroidal samples pre-annealed at 370, 380, 390, and 400 °C were designated as P370, P380, P390, and P400, respectively. Similarly, toroidal samples core annealed at 400, 425, 450, 475, and 500 °C were designated as C400, C425, C450, C475, and C500, respectively.

2.3. Characterization

The thermal properties of the Fe-Si-B ribbons were determined by differential scanning calorimetry (DSC) at a heating rate of 20 K/min in N_2 atmosphere. The crystalline structure of the ribbons after pre-annealing and of the flake powder after ball milling were analyzed using an X-ray diffractometer (XRD, D/Max 2500, Rigaku, Tokyo, Japan) with Cu Kα radiation. The particle sizes of flake powders were determined by a LASER particle size analyzer (LS13 320, Beckman Coulter, Brea, CA, USA). Tap density values of the flake powders were analyzed to determine the binder addition amount. The static magnetic properties of the flake powder were measured using a vibrating sample magnetometer (VSM, EZ9, MicroSense, Tempe, AZ, USA). The microstructure of the flake powder was observed using a field-emission scanning electron microscope (FE-SEM, MIRA3 LM, TESCAN, Brno, Czech Republic) equipped with an energy-dispersive X-ray spectroscope (EDS). The total core loss of the toroidal sample was measured using an AC B-H analyzer (SY-8219, IWATSU ELECTRIC, Tokyo, Japan) in a frequency range from 10 kHz to 1 MHz, with a maximum applied induction of 100 mT. The frequency-dependent permeability and DC bias properties of the toroidal sample were observed using an LCR meter (3260B, WAYNE KERR Electronics, Bognor Regis, UK). The flux density and coercive fields of the toroidal samples were measured by DC-B-H analyzer (Pemagraph c-500, Magnet-Physik, Köln, Germany) with applied field of -1 ± 1 kA/m.

3. Results and Discussion

As shown in Figure 1, the amorphous metal ribbon was pulverized into flake powder through pre-annealing, followed by milling processes. The ball milling process is a relatively low-energy process that has little potential to change the shape of the powder, such as through crumpling or edge wear. The ball milling speed is set below a threshold so that the ball falls at the maximum height and generates maximum impact energy [37]. The ball milling time is set to allow sufficient time for the ribbon to be pulverized into powder and to take into account the increased level of contamination due to a long time [38]. The pre-annealing temperature and ball milling process affect the size and shape of the pulverized particles, which are closely related to the magnetic properties. The pulverized flake powder was then formed into a toroidal-shaped core under high pressure compaction. Since amorphous powder does not have a plastic deformation mechanism, the core density may be low at low pressure, and therefore it was formed under high pressure. Core annealing can improve the magnetic properties by removing residual stresses formed during the pulverizing and pressing processes. This study aimed to investigate in detail the effects of pre-annealing and core annealing temperature on the size and shape of particles, and the magnetic properties of the composite such as permeability, core loss, and DC bias characteristics.

Ribbons and pulverized powders with different pre-annealing temperatures were analyzed, as shown in Figure 2. The crystallization behavior of the Fe-Si-B ribbon was evaluated using DSC, as shown in Figure 2a. The glass transition temperature (T_g) before crystallization was not clearly indicated, and the Curie temperature (T_c) and crystallization onset temperature (T_x) were confirmed to be 396 °C and 495 °C, respectively. The milling process can lead to a distribution of the Curie temperature [39], but a very subtle inflection point was observed at 396 °C. This value is similar to the one reported in the literature [13]. Two exothermic peaks were observed, indicating that crystallization occurred in two steps. The first crystallization step was observed at around 515 °C; this corresponds to α-Fe(Si) crystal formation [40]. The second crystallization step was observed at around 550 °C, and was due to intermetallic Fe_2B precipitation. The annealing, even at temperatures below the crystallization temperature, can have an impact on the soft magnetic properties of amorphous ribbons. This is attributed to the relief of stress accumulated during the rapid quenching process, atomic rearrangement such as chemical short-range ordering, and the initiation of nucleation of α-Fe crystallites [41]. The chemical short-range order of the amorphous structure induces local anisotropy, increasing the coercivity, but it can also increase the brittleness [22,42,43]. Heat treatment above the Curie temperature eliminates the chemical short-range order of the amorphous structure, so pre-annealing was carried out below the Curie temperature; core annealing was carried out above the Curie temperature and below the crystallization temperature.

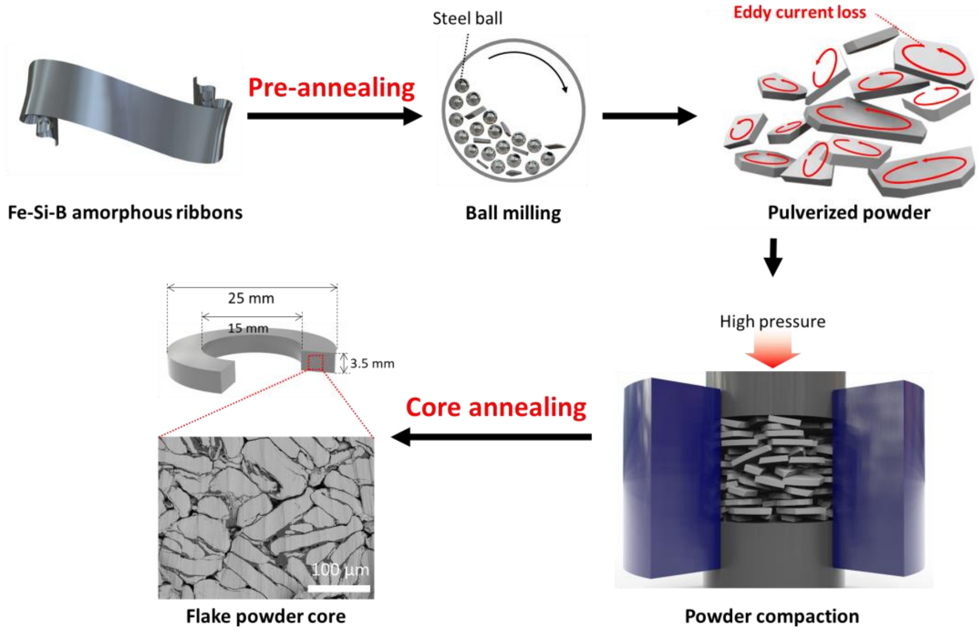

Figure 1. Schematic of soft magnetic composites manufactured using flake powder.

Therefore, the pre-annealing temperature was set in the range of 350–400 °C, which is lower than the Curie temperature. Figure 2b shows X-ray diffraction pattern results of the pre-annealed ribbon at 350–500 °C. A halo pattern was observed around 2θ = 45° for all samples. Ribbons pre-annealed at 500 °C show the α-Fe phase (JCPDF#87-0721) peak. It was observed that the ribbon pre-annealed above 370 °C easily broke when bent at 180°. The pre-annealed ribbon was pulverized using ball milling. As a result, the ribbon pre-annealed below 360 °C was not pulverized due to its high toughness, the results of its intrinsic amorphous properties. Therefore, it is suggested that the ribbon pre-annealed above 370 °C has sufficient brittleness to be pulverized into powder due to the formation of chemical short-range order. The ribbon pre-annealed above 370 °C was pulverized into powder and analyzed to determine its diffraction pattern (Figure 2c). No distinct crystalline peaks were observed in any of the samples. This shows that there is no influence of oxidation or impurities even after pre-annealing and pulverization processes, and the amorphous state is maintained. The particle sizes of the pulverized and pre-annealed flake powders were observed and are presented in Figure 2d. As the pre-annealing temperature increased in the range below the crystallization temperature, the brittleness of the amorphous alloy increased [22]. As a result, the particle size of the flake powder decreased as the pre-annealing temperature increased due to the formation of chemical short-range order, increasing the brittleness of the amorphous metal ribbon and improving the pulverization efficiency. The average particle sizes (D50) of the flake powders, which underwent pre-annealing at temperatures of 370 °C and 400 °C, were measured and found to be 115.8 μm and 96.4 μm, respectively.

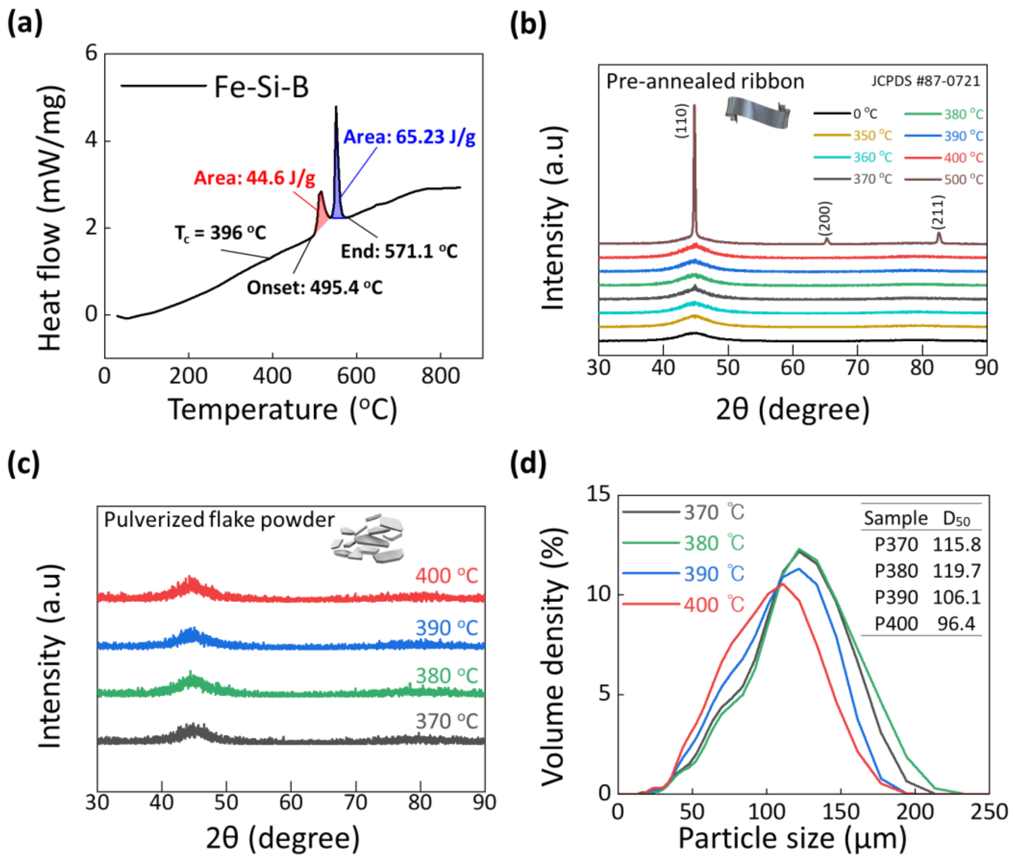

Figure 2. (**a**) Differential scanning calorimeter curves of Fe-Si-B ribbons. (**b**) X-ray diffractometer patterns of the Fe-Si-B ribbons before pre-annealing and Fe-Si-B ribbons pre-annealed at 350–500 °C. (**c**) X-ray diffractometer pattern and (**d**) particle size of flake powder after pre-annealing at 370–400 °C and ball milling.

Figure 3a–d show surface SEM images of pulverized powders with different pre-annealing temperatures. The shape of the pulverized powder particles appears as flakes. The results of particle size analysis also show a tendency for particle size to decrease as the pre-annealing temperature increases, as shown in Figure 2d. Some edges of the flake powder are slightly rounded due to the pulverization process, and the surfaces are rough. This tendency was more pronounced as the pre-annealing temperature increased and the pulverization efficiency increased.

Figure 4a shows hysteresis loops of flake powders with different pre-annealing temperatures analyzed by a vibrating sample magnetometer. All samples show typical S-shaped hysteresis loops. The saturation magnetization and coercivity of the flake powders prepared at different pre-annealing temperatures are shown in Figure 4b. Since ribbons with the same composition were used, there was no significant difference in saturation magnetization of the flake powders with different pre-annealing temperatures. The coercivity tended to increase gradually as the pre-annealing temperature increased. The saturation magnetization and coercivity of the flake powders pre-annealed at 400 °C were 179 emu/g (1.61 T) and 55.7 Oe, respectively.

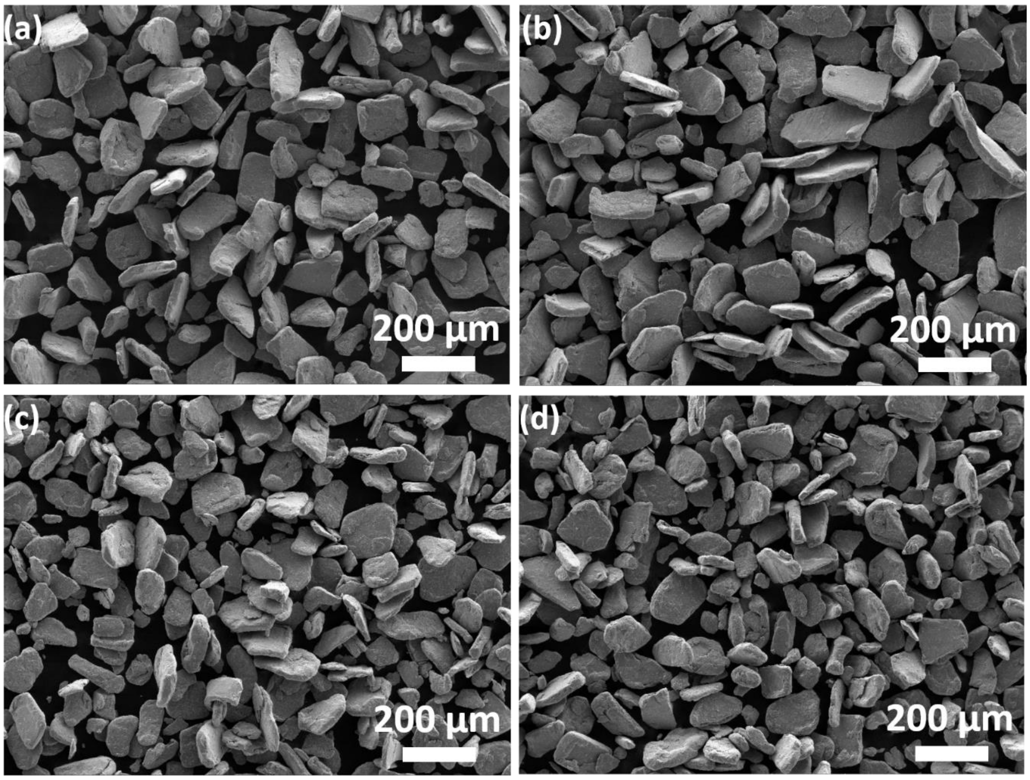

Figure 3. (**a**) Microstructure of ball-milled flake powders after pre-annealing at 370 °C, (**b**) 380 °C, (**c**) 390 °C, and (**d**) 400 °C.

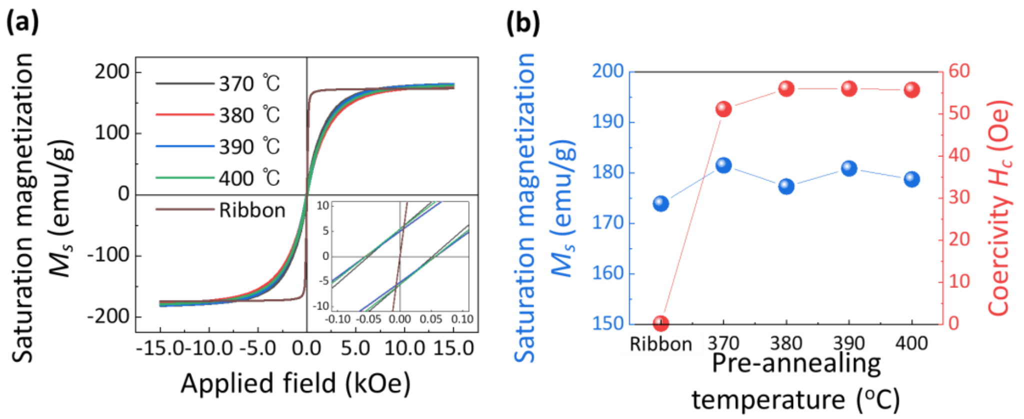

Figure 4. (**a**) Magnetic hysteresis loops and (**b**) saturation magnetization and coercivity of ball-milled flake powder after pre-annealing at 370–400 °C.

The cross-sectional microstructure of a toroidal core made of pulverized powder was observed, as shown in Figure 5. The white parts are flake powder; the black parts are additives such as potassium silicate and kenolube. Flake powders with maximum diameter of 90 μm and thickness of about 22 μm were partially arranged perpendicular to the molding direction. Therefore, as can also be seen in the microstructures shown in Figures 1 and 5, flake powder arranged vertically due to the process of pressing from top to bottom was not observed; horizontally arranged powder, however, was observed. This arrangement improved permeability due to the small demagnetizing field due to the shape magnetic anisotropy. The potassium silicate solution used as a binder contains Si, K, and O elements. Potassium silicate exhibits excellent adhesion throughout the curing process. It also plays an important role in insulation by forming polysilicates between particles. Therefore, potassium silicate is a factor that reduces inter-particle eddy currents between particles. As a result of EDS analysis, Si, K, and O elements were confirmed between the particles, confirming that potassium silicate was located between the particles.

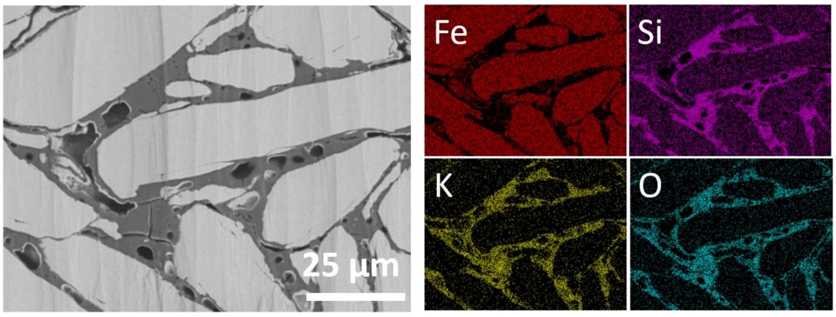

Figure 5. Cross-sectional SEM image and EDS element mapping results of toroidal sample pre-annealed at 400 °C and core annealed at 425 °C.

The magnetic properties of a toroidal sample made from flake powders with different pre-annealing temperatures were analyzed and results are shown in Figure 6. Figure 6a shows the core loss of the P370–P400 samples measured at maximum induction (B_m) = 20 mT and frequency (f) of 10–1000 kHz. As the pre-annealing temperature increased, the core loss tended to decrease; the P400 sample had the lowest core loss of 1019 kW/m^3 at f = 1000 kHz.

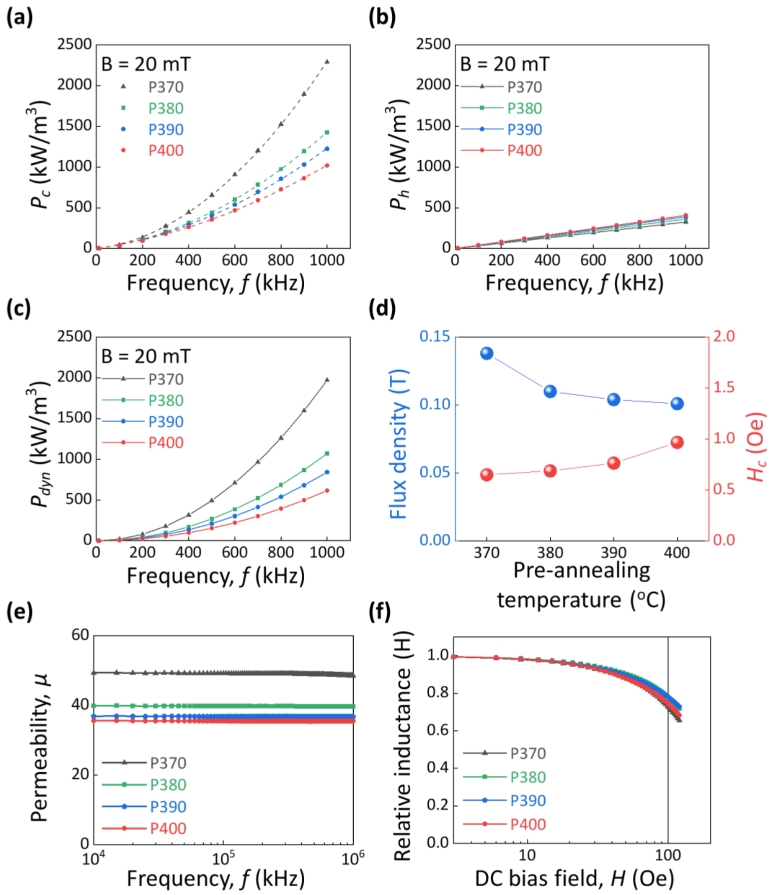

Figure 6. (**a**) Total core loss, (**b**) hysteresis loss, (**c**) dynamic loss, (**d**) magnetic flux density, coercivity (**e**) frequency dependence of permeability, and (**f**) relative inductance by amount of DC bias field of Fe-Si-B flake powder cores pre-annealed at 370–400 °C.

Total core loss (P_c) is composed of hysteresis loss (P_h), eddy current loss (P_e), and anomalous loss (P_a) per unit volume. Hysteresis loss is the energy corresponding to the internal area of the hysteresis loop and is expressed in Equation (1) [44].

$$P_h = C_h B_m^2 f \tag{1}$$

Here, C_h is hysteresis loss coefficient.

Eddy current is the electrical current induced in a direction that prevents magnetization according to Faraday's law of electromagnetic induction when a magnetic material is magnetized by an external alternating magnetic field. P_e can be expressed as Equation (2) [45].

$$P_e = K_e f^2 = \frac{(\pi d B_m f)^2}{c\rho} \tag{2}$$

Here, K_e is the coefficient of eddy current loss, d is the particle size, c is the specific heat capacity of the material, and ρ is the resistivity of the particle.

P_a is quite complex, because it includes relaxation loss and resonant loss. However, P_a was found to be proportional to the square of the frequency for amorphous SMCs [46].

Therefore, total core loss, P_c, can be simply expressed as Equation (3) [47,48].

$$P_c = P_h + P_e + P_a = K_h f + K_e f^2 + K_a f^2 = K_h f + K_{dyn} f^2 \tag{3}$$

Here, K_{dyn} is the dynamic loss coefficient. The dynamic loss comprises both the eddy current loss and anomalous loss.

The frequency-dependent core losses of the P370–P400 samples were fitted using Equation (3); the results are shown as dotted lines in Figure 6a. The experimental data and predicted results match well. Using Equation (3), the coefficients of hysteresis and dynamic losses were obtained: the core losses of the P370–P400 samples, measured at B_m = 20 mT and f = 10–1000 kHz, were classified into hysteresis and dynamic losses, in Figures 6b and 6c, respectively. As the pre-annealing temperature increased, the total core loss decreased (Figure 6a), the hysteresis loss increased (Figure 6b), and the dynamic loss decreased (Figure 6c).

As the pre-annealing temperature increases, the properties of the powder may deteriorate due to the accumulation of milling damage. As a result, hysteresis loss will increase. As can be seen in Figure 6d, the coercivity increased as the pre-annealing temperature increased. In contrast, as the particle size decreased, the dynamic loss within the particles decreased. The anomalous loss is related to eddy currents formed around the domain walls [49]. By enhancing the pulverization efficiency, particle size reduction is achieved. Therefore, the movement of domain walls can be reduced, resulting in a reduction in anomalous loss. Although the hysteresis loss increased as the pre-annealing temperature increased, the sample pre-annealed at 400 °C showed the lowest core loss at high frequencies due to the sharp decrease in dynamic loss.

Figure 6e shows the permeability according to the frequency for the P370–P400 samples from 10 kHz to 1 MHz. The permeability of the P370 sample was the highest; it gradually decreased as the pre-annealing temperature increased. As can be seen in Figure 3, as the particle size decreased, the aspect ratio of the particles also decreased. This increases the likelihood of particles being arranged perpendicular to the field, which increases the demagnetization factor and decreases the permeability.

The DC bias characteristics of the P370–P400 sample were analyzed and are shown in Figure 6f. In general, the DC bias characteristics tend to increase as permeability decreases. On the other hand, when the permeability decreases (Figure 6d), the DC bias tends to increase. Due to the sharp decrease in permeability, the DC bias increased from P370 to P390; however, for P400, at which the decrease in permeability is less, the DC bias decreased again.

Table 1 summarizes the magnetic properties such as density, coercivity, permeability, core loss, and DC bias of P370–P400 samples. As the pre-annealing temperature increased, magnetic flux density and permeability decreased while coercivity increased. The core loss at relatively low frequencies, f = 100 kHz and B_m = 100 mT, tended to gradually increase as the pre-annealing temperature increased, because hysteresis loss was dominant. On the other hand, at high frequency f = 1 MHz and B_m = 20 mT, dynamic loss was dominant, showing a gradual decrease as pre-annealing temperature increased. The P370–P400 samples maintained a level of inductance of 73–78% at a DC bias field of 100 Oe. Therefore, since the core loss was the lowest at the pre-annealing temperature of 400 °C in the high frequency range, core annealing was carried out after fixing the temperature at 400 °C.

Table 1. Summary of density and soft magnetic properties of Fe-Si-B flake powder cores prepared with ribbons pre-annealed at 370–400 °C.

Sample	Density (g/cm^3)	Relative Density (%)	Flux Density (T)	H_c (Oe)	Permeability	P_c (kW/m^3)	P_c (kW/m^3)	DC Bias (%)
					f = 1 MHz	100 kHz/ 100 mT	1 MHz/ 20 mT	100 Oe
P370	5.3310	74.25	0.138	0.6497	48.45	1630	2288	73.04
P380	5.3330	74.28	0.110	0.6886	39.67	1604	1424	78.21
P390	5.2635	73.31	0.104	0.7640	36.68	1470	1225	78.24
P400	5.6103	78.14	0.102	0.9676	35.46	1876	1091	74.61

Figure 7 shows the total core loss per unit volume, eddy current loss, hysteresis loss, effective permeability, and DC bias of the C400–C500 samples. Figure 7a shows the core losses of the C400–C500 samples measured at B_m = 20 mT and f = 10–1000 kHz. C500 showed the highest core loss, while C425 showed the lowest. Samples annealed at temperatures above 425 °C showed an increasing trend in core loss as the core annealing temperature increased. The results, fitted using Equation (3), are shown as dashed lines; they match well with the experimental data. The core loss values of the C400–C500 samples measured at B_m = 20 mT and f = 10–1000 kHz were classified according to the coefficients of hysteresis and dynamic loss, as shown in Figures 7b and 7c, respectively. In Figure 7b, it can be seen that the hysteresis loss decreased until the core annealing temperature reached 450 °C, and then increased again. As can also be seen in Figure 7d, the lowest coercivity was observed at a core annealing temperature of 450 °C, and the trend of coercivity was similar to that of hysteresis loss. Crystallization resulting from annealing at temperatures above 475 °C caused an increasing trend in hysteresis loss. As shown in Figure 7c, dynamic loss decreased until the core annealing temperature reached 425 °C, and then increased again. Residual stresses generated during the pressing process can be adequately eliminated by core annealing at temperatures above 425 °C.

The effective permeability of the C400–C500 samples was analyzed according to frequency from 10 kHz to 1 MHz, with results shown in Figure 7e. The effective permeability values of all samples were maintained up to f = 1 MHz, with no sharp decreases. The magnetic flux density values according to the core annealing temperature are shown in Figure 7d; these values were high at 425 °C and 450 °C and then decreased as the temperature increased. This trend was similar to that of the effective permeability, shown in Figure 7e; the C425 and C450 samples have about 35 high and stable effective permeability. The effective permeability of samples annealed above 475 °C decreased dramatically due to crystallization.

The DC bias characteristics of the C400–C500 samples with different core annealing temperatures are shown in Figure 7f. The C400–C500 samples showed a maintenance level of 74–93% of inductance at a DC bias field of 100 Oe. Generally, DC bias characteristics are known to decrease as the effective permeability increases. Therefore, the DC bias characteristics of the C400–C500 samples showed a tendency opposite to the permeability.

Table 2 shows values of magnetic properties such as density, coercivity, permeability, core loss, and DC bias of the C400–C500 samples. Core annealing at 425 °C and 450 °C led to excellent permeability and DC bias characteristics. The core loss at relatively low frequencies of f = 100 kHz and B_m = 100 mT was dominated by hysteresis loss, with the lowest core loss at 450 °C. On the other hand, at high frequencies of f = 1 MHz and B_m = 20 mT, dynamic loss was dominant, with the lowest core loss at 425 °C.

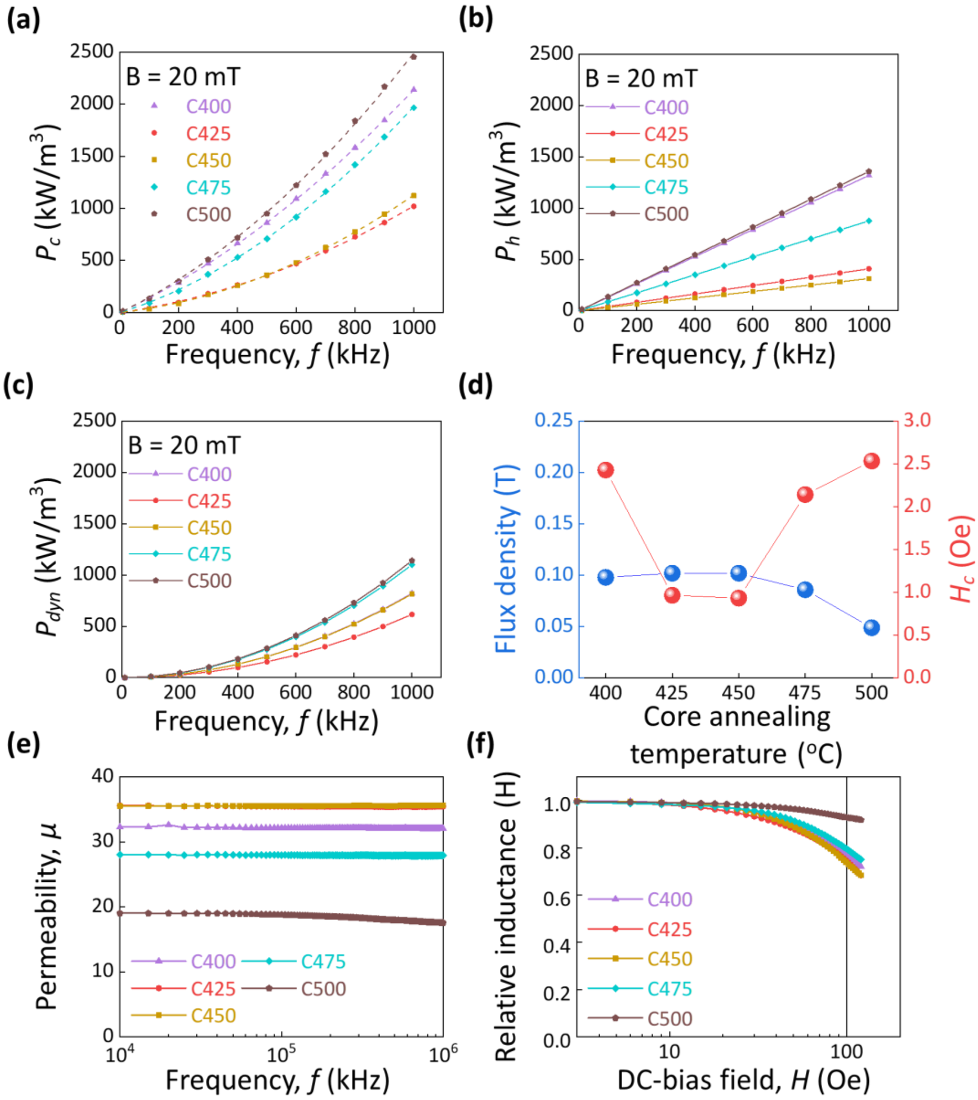

Figure 7. (**a**) Total core loss, (**b**) hysteresis loss, (**c**) dynamic loss, (**d**) magnetic flux density, coercivity (**e**) frequency dependence of permeability, and (**f**) relative inductance by amount of DC bias field of Fe-Si-B flake powder cores after core annealing at 400–500 °C.

Table 2. Summary of density and soft magnetic properties of Fe-Si-B flake powder cores prepared with core annealing at 400–500 °C.

Sample	Density (g/cm^3)	Relative Density (%)	Flux Density (T)	H_c (Oe)	Permeability	P_c (kW/m^3)	P_c (kW/m^3)	DC Bias (%)
					f = 1 MHz	100 kHz/ 100 mT	1 MHz/ 20 mT	100 Oe
C400	5.5057	76.68	0.098	2.4291	32.01	6016	2139	77.16
C425	5.6103	78.14	0.102	0.9676	35.46	1876	1091	74.61
C450	5.3250	74.16	0.102	0.9337	35.63	1693	1123	73.81
C475	5.1699	72.00	0.086	2.1426	27.91	5401	1966	79.63
C500	5.1392	71.58	0.049	2.5346	17.54	–	2453	92.84

4. Conclusions

Fe-Si-B ribbons were successfully pulverized using pre-annealing and ball milling processes, resulting in flake-shaped powders. As the pre-annealing temperature increased, the brittleness of the ribbons increased, leading to an increase in pulverization efficiency and a decrease in particle size. Through high-pressure molding and core annealing, toroidal cores were manufactured using flake powders, and their magnetic properties, such as permeability, core loss, and DC bias characteristics were closely examined. Our results indicate that increasing the pre-annealing temperature reduced particle size, effectively diminishing eddy current loss. Furthermore, conducting core annealing at temperatures between 425 °C and 475 °C eliminated residual stress without forming crystals, thus enhancing the magnetic properties. In conclusion, an SMC pre-annealed at 400 °C and core-annealed at 425 °C demonstrated high permeability (μ = 35) and low core loss (P_{cv} = 1091 kW/m^3 at f = 1 MHz with B_m = 20 mT), along with excellent DC bias characteristics (75% at 100 Oe). Our findings suggest that temperature control during the annealing process is an effective way to improve the magnetic properties of flake powder cores with high saturation magnetization.

Author Contributions: Investigation, writing—original draft, H.-R.K. and D.L.; Methodology and magnetic characterization, S.Y. and Y.-T.K.; writing—review and editing, J.K. and Y.K.; Conceptualization, writing—review and editing, supervision, J.-W.J. All authors have read and agreed to the published version of the manuscript.

Funding: This work was supported by Steel Re-Leap Project and Automotive Technology Development Project funded by the Korea Ministry of Trade, Industry and Energy (MOTIE, Republic of Korea). [Project number: 20015645 and 20018921].

Data Availability Statement: Data are contained within the article.

Conflicts of Interest: The authors declare no conflict of interest.

References

1. Hsiang, H.-I. Progress in materials and processes of multilayer power inductors. *J. Mater. Sci. Mater. Electron.* **2020**, *31*, 16089–16110. [CrossRef]
2. Zhou, B.; Dong, Y.; Chi, Q.; Zhang, Y.; Chang, L.; Gong, M.; Huang, J.; Pan, Y.; Wang, X. Fe-based amorphous soft magnetic composites with SiO2 insulation coatings: A study on coatings thickness, microstructure and magnetic properties. *Ceram. Int.* **2020**, *46*, 13449–13459. [CrossRef]
3. Woo, H.J.; Ahn, J.H.; Kim, C.P.; Choi, D.H.; Kim, S.; Lee, B.W. Effect of the particle size classification of FeSiCrB amorphous soft magnetic composites to improve magnetic properties of power inductors. *J. Non-Cryst. Solids.* **2022**, *577*, 121309. [CrossRef]
4. Chen, Y.; Zhang, L.; Sun, H.; Chen, F.; Zhang, P.; Qu, X.; Fan, E. Enhanced magnetic properties of iron-based soft magnetic composites with phosphate-polyimide insulating layer. *J. Alloys Compd.* **2020**, *813*, 152205. [CrossRef]
5. Thorsson, L.; Unosson, M.; Pérez-Prado, M.T.; Jin, X.; Tiberto, P.; Barrera, G.; Adam, B.; Neuber, N.; Ghavimi, A.; Frey, M. Selective laser melting of a Fe-Si-Cr-BC-based complex-shaped amorphous soft-magnetic electric motor rotor with record dimensions. *Mater. Des.* **2022**, *215*, 110483. [CrossRef]
6. Krings, A.; Cossale, M.; Tenconi, A.; Soulard, J.; Cavagnino, A.; Boglietti, A. Characteristics comparison and selection guide for magnetic materials used in electrical machines. In Proceedings of the 2015 IEEE International Electric Machines & Drives Conference (IEMDC), Coeur d'Alene, ID, USA, 10–13 May 2015; pp. 1152–1157.
7. Leary, A.M.; Ohodnicki, P.R.; McHenry, M.E. Soft magnetic materials in high-frequency, high-power conversion applications. *JOM* **2012**, *64*, 772–781. [CrossRef]
8. Inoue, A. Stabilization of metallic supercooled liquid and bulk amorphous alloys. *Acta Mater.* **2000**, *48*, 279–306. [CrossRef]
9. Azuma, D.; Ito, N.; Ohta, M. Recent progress in Fe-based amorphous and nanocrystalline soft magnetic materials. *J. Magn. Magn. Mater.* **2020**, *501*, 166373. [CrossRef]
10. Alvarez, K.L.; Baghbaderani, H.; Martín, J.; Burgos, N.; Ipatov, M.; Pavlovic, Z.; McCloskey, P.; Masood, A.; Gonzalez, J. Novel Fe-based amorphous and nanocrystalline powder cores for high-frequency power conversion. *J. Magn. Magn. Mater.* **2020**, *501*, 166457. [CrossRef]
11. Manchón-Gordón, A.F.; Ipus, J.J.; Blázquez, J.S.; Conde, C.F.; Conde, A.; Svec Sr, P. Study of the kinetics and products of the devitrification process of mechanically amorphized Fe70Zr30 alloy. *J. Alloys Compd.* **2020**, *825*, 154021. [CrossRef]
12. Manchón-Gordón, A.F.; Svec, P.; Ipus, J.J.; Kowalczyk, M.; Blázquez, J.S.; Conde, C.F.; Conde, A.; Svec, P.; Kulik, T. Devitrification of mechanically alloyed Fe-Nb system: Mössbauer study of the intermetallic phases. *Metall. Mater. Trans. A* **2020**, *51*, 1395–1401. [CrossRef]

13. Metglas®, Inc. Available online: https://metglas.com/magnetic-materials/ (accessed on 6 December 2023).
14. Şimşek, T. Investigation of the structural and magnetic properties of Fe70Ti10B20 (at.%) alloys by mechanical alloying. *J. Boron* **2019**, *4*, 85–91.
15. Saji, S.; Abe, S.; Matsumoto, K. Formation Process of Amorphous Phase during Mechanical Alloying for Al-6 and 12 AT% Ti Mixed Powders. In *Materials Science Forum*; Trans Tech Publications Ltd.: Stafa-Zurich, Switzerland, 1992; pp. 367–374.
16. Enayati, M.; Mohamed, F. Application of mechanical alloying/milling for synthesis of nanocrystalline and amorphous materials. *Int. Mater. Rev.* **2014**, *59*, 394–416. [CrossRef]
17. Li, G.; Shi, G.; Miao, H.; Liu, D.; Li, Z.; Wang, M.; Wang, L. Effects of the Gas-Atomization Pressure and Annealing Temperature on the Microstructure and Performance of FeSiBCuNb Nanocrystalline Soft Magnetic Composites. *Materials* **2023**, *16*, 1284. [CrossRef] [PubMed]
18. Zdrodowska, K.; Kwarciak, P.; Jędryka, J.; Szota, M.; Nabiałek, M. Thin-layered amorphous Fe73Co5Y3B19 strip produced by the melt-spinning method. *Inżynieria Mater.* **2013**, *34*, 401–404.
19. Lawley, A. Fundamentals of Particulate Metallurgy. In *Advances in Metal Processing*; Springer: Boston, MA, USA, 1981; pp. 91–109.
20. Luborsky, F.E. Magnetic properties of amorphous alloys. *J. Magn. Magn. Mater.* **1978**, *7*, 143–149. [CrossRef]
21. Herzer, G. Modern soft magnets: Amorphous and nanocrystalline materials. *Acta Mater.* **2013**, *61*, 718–734. [CrossRef]
22. Liu, X.; Wang, T.; Wang, Q.; Song, X.; Liang, Y.; Feng, S.; Yang, F.; Chen, X.; Kong, J. Shear band evolution related with thermal annealing revealing ductile-brittle transition of Zr35Ti30Be27. 5Cu7. 5 metallic glass under complex stress state. *Intermetallics* **2022**, *140*, 107378. [CrossRef]
23. Suzuki, K.; Ito, N.; Saranu, S.; Herr, U.; Michels, A.; Garitaonandia, J. Magnetic domains and annealing-induced magnetic anisotropy in nanocrystalline soft magnetic materials. *J. Appl. Phys.* **2008**, *103*, 07E730. [CrossRef]
24. Basova, T.V.; Jushina, I.V.; Ray, A.K. Influence of post-deposition annealing under magnetic field on the structure of phthalocyanine thin films. *J. Mater. Sci. Mater. Electron.* **2015**, *26*, 4716–4721. [CrossRef]
25. Guo, X.; Liu, L.; Yao, B. Structural Characterization and Properties of Fe-N SMCS Prepared by Reaction Between Fe and BN During Ball Milling. *J. Jilin Univ. Sci. Ed.* **2008**, *46*, 535–538.
26. Nowosielski, R.; Wysłocki, J.; Wnuk, I.; Gramatyka, P. Nanocrystalline soft magnetic composite cores. *J. Mater. Process. Technol.* **2006**, *175*, 324–329. [CrossRef]
27. Yang, Y.; Wang, Y.; Wu, S.; Liu, C.; Chen, L. Core loss analysis of soft magnetic composites considering the inter-particle eddy current loss. *AIP Adv.* **2021**, *11*, 015140. [CrossRef]
28. Lisjak, D.; Mertelj, A. Anisotropic magnetic nanoparticles: A review of their properties, syntheses and potential applications. *Prog. Mater. Sci.* **2018**, *95*, 286–328. [CrossRef]
29. Manchón-Gordón, A.F.; Ipus, J.; Moreno-Ramírez, L.M.; Blázquez, J.; Conde, C.; Franco, V.; Conde, A. Correction of the shape effect on magnetic entropy change in ball milled Fe70Zr30 alloys. *J. Alloys Compd.* **2018**, *765*, 437–443. [CrossRef]
30. Ma, R.; Chang, L.; Ye, S.; Xie, H.; Xiao, Q.; Zhang, L.; Si, J.; Yu, P. Magnetic properties of soft magnetic composites fabricated from amorphous Fe73Si11B11C3Cr2 powder by hot pressing under a low pressure. *Powder Technol.* **2023**, *426*, 118639. [CrossRef]
31. Egami, T. Structural relaxation in amorphous alloys-compositional short range ordering. *Mater. Res. Bull.* **1978**, *13*, 557–562. [CrossRef]
32. Strečková, M.; Füzer, J.; Kobera, L.; Brus, J.; Fáberová, M.; Bureš, R.; Kollár, P.; Lauda, M.; Medvecký, Ĺ.; Girman, V. A comprehensive study of soft magnetic materials based on FeSi spheres and polymeric resin modified by silica nanorods. *Mater. Chem. Phys.* **2014**, *147*, 649–660. [CrossRef]
33. Ding, W.; Jiang, L.; Li, B.; Chen, G.; Tian, S.; Wu, G. Microstructure and magnetic properties of soft magnetic composites with silicate glass insulation layers. *J. Supercond. Nov. Magn.* **2014**, *27*, 239–245. [CrossRef]
34. Zhang, Z.; Xu, W.; Guo, T.; Jiang, Y.; Yan, M. Effect of processing parameters on the magnetic properties and microstructures of molybdenum permalloy compacts made by powder metallurgy. *J. Alloys Compd.* **2014**, *594*, 153–157. [CrossRef]
35. Ramamurty, U.; Lee, M.; Basu, J.; Li, Y. Embrittlement of a bulk metallic glass due to low-temperature annealing. *Scripta Mater.* **2002**, *47*, 107–111. [CrossRef]
36. Kumar, G.; Rector, D.; Conner, R.; Schroers, J. Embrittlement of Zr-based bulk metallic glasses. *Acta Mater.* **2009**, *57*, 3572–3583. [CrossRef]
37. Suryanarayana, C. Mechanical alloying and milling. *Prog. Mater Sci.* **2001**, *46*, 1–184. [CrossRef]
38. Suryanarayana, C. Does a disordered γ-TiAl phase exist in mechanically alloyed TiAl powders? *Intermetallics* **1995**, *3*, 153–160. [CrossRef]
39. Manchón-Gordón, A.F.; López-Martín, R.; Vidal-Crespo, A.; Ipus, J.J.; Blázquez, J.S.; Conde, C.F.; Conde, A. Distribution of transition temperatures in magnetic transformations: Sources, effects and procedures to extract information from experimental data. *Metals* **2020**, *10*, 226. [CrossRef]
40. Huang, B.; Perez, R.; Crawford, P.; Sharif, A.; Nutt, S.; Lavernia, E. Mechanically induced crystallization of metglas Fe78B13Si9 during cryogenic high energy ball milling. *Nanostruct. Mater.* **1995**, *5*, 545–553. [CrossRef]
41. Manchón-Gordón, A.; Blázquez, J.; Kowalczyk, M.; Ipus, J.; Kulik, T.; Conde, C. Effect of thermal treatments below devitrification temperature on the magnetic and magnetocaloric properties in mechanically alloyed Fe70Zr30 powders. *J. Non-Cryst. Solids.* **2023**, *609*, 122267. [CrossRef]

42. Walter, J.; Bacon, F.; Luborsky, F. An Auger analysis of the embrittlement of the amorphous alloy Ni40Fe40P14B6. *Mater. Sci. Eng.* **1976**, *24*, 239–245. [CrossRef]
43. Ghaemi, M.; Jafary-Zadeh, M.; Khoo, K.H.; Gao, H. Chemical affinity can govern notch-tip brittle-to-ductile transition in metallic glasses. *Extrem. Mech. Lett.* **2022**, *52*, 101651. [CrossRef]
44. Chen, Y.; Pillay, P. An Improved formula for lamination core loss calculations in machines operating with high frequency and high flux density excitation. In Proceedings of the Conference Record of the 2002 IEEE Industry Applications Conference: 37th IAS Annual Meeting (Cat. No. 02CH37344), Pittsburgh, PA, USA, 13–18 October 2002; pp. 759–766.
45. Yaghtin, M.; Taghvaei, A.H.; Hashemi, B.; Janghorban, K. Effect of heat treatment on magnetic properties of iron-based soft magnetic composites with Al2O3 insulation coating produced by sol–gel method. *J. Alloys Compd.* **2013**, *581*, 293–297. [CrossRef]
46. Cao, P.; Liu, Y.; Li, J.; Du, J.; Wang, R.; Zhou, T. Enhanced magnetic properties of hot-pressed Fe-based nanocrystalline powder cores with low-melted glass-modified insulating. *IEEE Trans. Magn.* **2021**, *57*, 2800407. [CrossRef]
47. Xie, D.-Z.; Lin, K.-H.; Lin, S.-T. Effects of processed parameters on the magnetic performance of a powder magnetic core. *J. Magn. Magn. Mater.* **2014**, *353*, 34–40. [CrossRef]
48. Yang, B.; Li, X.; Guo, R.; Yu, R. Oxidation fabrication and enhanced soft magnetic properties for core-shell FeCo/CoFe2O4 micron-nano composites. *Mater. Des.* **2017**, *121*, 272–279. [CrossRef]
49. Perigo, E.A.; Weidenfeller, B.; Kollár, P.; Füzer, J. Past, present, and future of soft magnetic composites. *Appl. Phys. Rev.* **2018**, *5*, 031301. [CrossRef]